A Fully Pneumatic Soft Manipulator with Proximally Generated, Body-Transmitted Roll for Closed-Loop 6-DoF Pose Regulation

Yusong Jin[1†], Hao Jiang[1†*], Feng Wu[1*], Keke Tang[2], Shiqi Zhang[3], and Xiaoping Chen[1,4]

***Abstract*— Most soft manipulators lack independently controllable roll about the end-effector's longitudinal axis, leaving the complete pose unregulated. Roll can instead be generated at the arm base and transmitted through the deformable body, avoiding both a distal rotary actuator and a routed transmission element—a route so far demonstrated at surgical scale and at mN·m torque levels. We extend it to a manipulation-scale, fully pneumatic platform in which a base-mounted pneumatic rotary actuator drives rotation and coordinated deformation of a torsionally stiff honeycomb arm converts it into end-effector roll. At this scale the architecture becomes markedly harder to control. We therefore develop a spherical-joint-approximation model with explicit passive torsion coordinates and a progress-based kinematic synchronization (PBKS) strategy. Across 30 workspace targets under four control configurations, the full framework satisfied 2 mm / 1° at $t = 30$ s at every target, whereas a torsion-free model failed on 16/30 targets and disabling synchronization raised the mean position overshoot from 8 to 212 mm. The arm tracked a 180° end-effector roll while regulating the remaining five DoFs, and delivered 6 – 10.5 N·m of blocked-output roll torque. Door unlocking, lightbulb installation, and water pouring illustrate task feasibility in the tested quasi-static regime.**

I. Introduction

Soft arms offer superior compliance and contact safety in unstructured environments [1], [2], yet most provide only five controllable degrees of freedom (DoFs)—three translational and two rotational—and lack an independently controllable *roll* about the end-effector's longitudinal axis [3]–[5]. This limitation makes roll-critical tasks such as pouring water, screwing in lightbulbs, and turning door handles infeasible under fixed-position and approach-direction constraints and, more generally, prevents independent regulation of the complete end-effector pose.

Three routes have been explored to introduce roll. The first integrates a dedicated rotary module at the distal end [6], [7], at the cost of additional moving mass and rotational inertia. The second transmits base-actuator rotation through cables [8], [9] or nested metamaterial structures [10] and has achieved unified 6-DoF closed-loop control [9], but requires transmission elements routed along the arm and motor-driven roll. The third route requires neither distal rotary hardware nor a routed transmission: the arm is rotated at its base while its bending-plane azimuths reconfigure oppositely to compensate the resulting sweep and produce tool roll [11]–[14]. The tradeoff is that the arm body becomes the torque-transmission path and must reconfigure in coordination with proximal rotation throughout the motion.

This last route has been investigated predominantly in surgical-scale continuum manipulators. Kong *et al.* [11] demonstrated single-section in-situ roll by rotating the actuation module together with the arm base while preserving the end-effector position and approach direction. Zhao *et al.* extended this principle to a dual-segment pneumatic continuum arm [12], and later regulated the three-dimensional tip position in closed loop with concurrently commanded backbone rotation [13]. Gao *et al.* [14] used offline-identified feedforward compensation to reconstruct the pose of a two-segment tendon-driven manipulator. These systems address constrained in-situ roll or position–rotation coordination, and all use motorized proximal rotation. Kong and Gao report end-effector torques of approximately 30.8 and 200 mN·m respectively [11], [14].

Bringing this architecture to a large-scale, load-bearing multisegment soft manipulator for everyday tasks is not a straightforward scale-up of the systems above. Firstly, unlike a distal rotary joint that directly provides a dedicated tool-axis roll coordinate, proximal rotation changes both the position and orientation of a bent arm, and local tool roll emerges only through coordinated multisegment reconfiguration. Because noncoplanar bending across segments can itself contribute to end-effector roll, a torsion-free inverse model misallocates arm-side roll residuals to active bending, progressively distorting the arm shape even in free-space regulation. At the N·m-scale loads targeted here, passive body twist further widens the mismatch between the real arm and a bending-only model, amplifying this misallocation and degrading the deliverable roll torque. Secondly, proximal rotation sweeps the entire bent arm, requiring multisegment reconfiguration to preserve the other five pose coordinates. Proximal rotation and multisegment reconfiguration differ in kinematic mapping and actuation response, so a mismatch in their progress causes transient pose errors. The translational error grows approximately with the end-effector's radial distance from the rotation axis; a mismatch tolerable at small scale can therefore become control-critical in a large, laterally extended arm. Progress must thus be coordinated throughout the motion, not merely at the endpoint.

† Both of the authors contributed equally. * Corresponding authors: Feng Wu (e-mail: wufeng02@ustc.edu.cn) and Hao Jiang (jhjh@mail.ustc.edu.cn).

[1]School of Computer Science and Technology, University of Science and Technology of China, Hefei, 230026, China.

[2]Cyberspace Institute of Advanced Technology, Guangzhou University, Guangzhou, 510006, China.

[3]School of Computing, The State University of New York (SUNY) at Binghamton, Binghamton, NY 13902, USA.

[4] The Guangdong Institute of Intelligent Manufacturing, GDAS, Guangdong, 510070, China.

This work was supported in part by the Major Research Plan of the National Natural Science Foundation of China under Grant 92048301 and in part by the Anhui Provincial Natural Science Foundation under Grant 2208085MF172.

This work realizes closed-loop regulation of all six end-effector pose coordinates in a fully pneumatic soft manipulator whose roll is generated proximally and transmitted through the arm body. The main contributions of this work are:

- **Manipulation-scale proximal roll transmission.** We extend this architecture from surgical-scale, mN·m systems to everyday manipulation, using a torsionally stiff honeycomb arm as the torque-transmission path. Blocked-output tests measured 6–10.5 N·m of whole-body end-effector roll torque, over an order of magnitude above prior body-transmitted implementations [11], [14].
- **Torsion-aware kinematic representation.** Explicit passive torsion coordinates prevent arm-side roll residuals from being misallocated to active multisegment bending. Compared with the torsion-free model, high-accuracy failures decreased from 16/30 to 0/30, while blocked-output roll torque increased from below approximately 3 to approximately 10 N·m at the tested constrained posture.
- **Progress-based kinematic synchronization.** PBKS coordinates proximal rotation with multisegment arm reconfiguration, reducing the across-target mean position overshoot from 212 to 8 mm while retaining comparable steady-state accuracy.

II. Task-Space Completeness and System Design

This section first presents a kinematic construction that introduces the missing independent roll coordinate through coordinated proximal rotation and arm reconfiguration (Sec. II-A). It then describes our fully pneumatic realization for load-bearing roll (Sec. II-B).

A. Proximal Rotation for Task-Space Completeness

Building on the proximal-roll route reviewed in Sec. I, Fig. 1 illustrates, using a single bending section, the kinematic construction that converts proximal rotation into local end-effector roll. Let $\boldsymbol{T}^{\text{arm}}$ denote the end-effector pose relative to the arm base in the initial state (Fig. 1(a)). Proximal rotation by δ alone left-multiplies the arm pose, yielding $\mathbf{R}_z(\delta)\boldsymbol{T}^{\text{arm}}$; this sweeps the entire bent section azimuthally and changes both the end-effector position and approach direction (Fig. 1(b)). Conversely, with the base fixed, reconfiguring the section through bending so that its bending-plane azimuth shifts by $-\delta$ produces the opposite sweep (Fig. 1(c)). For an ideal section whose kinematics are equivariant to azimuth shifts, the resulting arm-relative pose is $\tilde{\boldsymbol{T}}^{\text{arm}} = \mathbf{R}_z(-\delta)\boldsymbol{T}^{\text{arm}}\mathbf{R}_z(\delta)$. Here, the left- and right-multiplying rotations act in the arm-base and end-effector-local frames, respectively.

Performing both motions together therefore gives

$$\mathbf{R}_z(\delta)\tilde{\boldsymbol{T}}^{\text{arm}} = \mathbf{R}_z(\delta)\mathbf{R}_z(-\delta)\boldsymbol{T}^{\text{arm}}\mathbf{R}_z(\delta) = \boldsymbol{T}^{\text{arm}}\mathbf{R}_z(\delta), \quad (1)$$

which is equivalent to right-multiplying the initial pose by a local tool roll: the ideal world-frame centerline is preserved while an end-effector roll of δ remains (Fig. 1(d)).

For a multisegment arm, the same construction applies by shifting each section's bending-plane azimuth by $-\delta$ in its local upstream frame, while keeping its bending magnitude and length unchanged. This section-wise uniform shift is a sufficient, but not unique, construction for preserving the world-frame centerline while generating local end-effector roll. It establishes the kinematic basis for task-space completeness—coordinated proximal rotation and arm reconfiguration provide the missing independent roll coordinate—rather than imposing a section-level constraint on the controller, which regulates the complete end-effector pose under external feedback.

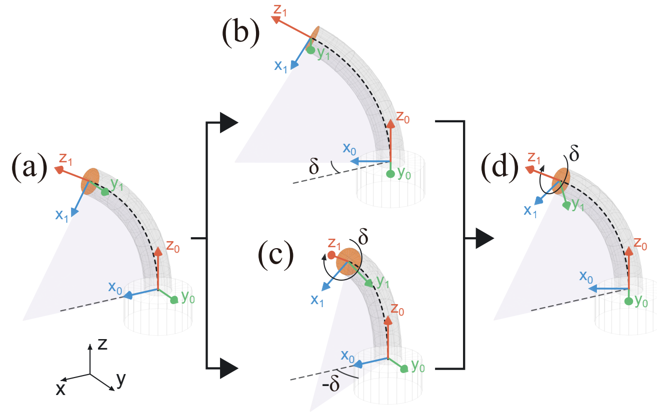

Fig. 1. Principle of proximal roll generation illustrated using a single bending section. (a) Initial configuration. (b) Proximal rotation by $+\delta$ produces an azimuthal sweep. (c) Changing the bending-plane azimuth by $-\delta$ produces the opposite sweep. (d) Combining the two motions preserves the world-frame centerline while producing local end-effector roll of δ.

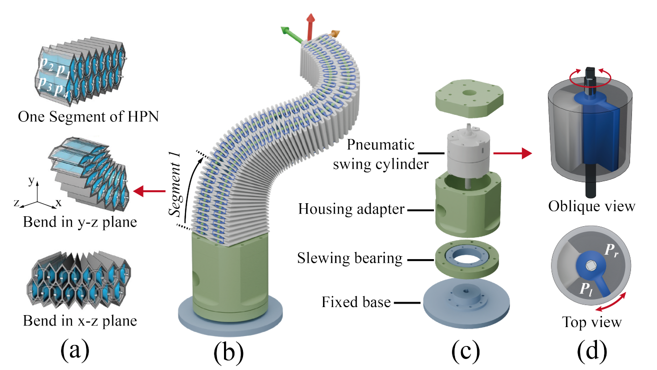

Fig. 2. Design of the proposed 6-DoF soft robotic arm. (a) Structure of a single Honeycomb Pneumatic Network (HPN) segment. (b) The complete system, composed of a four-segment HPN arm and a base rotary mechanism. (c) The rotary mechanism, consisting of a slewing bearing and a pneumatic swing rotary cylinder. (d) Schematic of the rotary cylinder.

B. Fully Pneumatic Realization for Load-Bearing Roll

The construction in Sec. II-A is purely kinematic. In a physical, load-bearing system, the deformable arm must transmit the proximal roll torque to the end effector. Our realization (Fig. 2) therefore combines an arm that is compliant in bending yet relatively stiff in torsion with a base-mounted pneumatic rotary actuator and a load-decoupling slewing bearing. This yields a fully pneumatic system without distal rotary hardware or a dedicated internal roll-transmission element.

Soft arm. The arm is based on the honeycomb pneumatic network (HPN) [3], [15], which is not claimed here as a new actuator design. Across its four segments the measured

TABLE I

GEOMETRIC AND MECHANICAL PARAMETERS OF THE FOUR SEGMENTS

Parameter	Seg 1	Seg 2	Seg 3	Seg 4
Wall thickness (mm)[a]	3.5	3.0	2.5	2.0
Airbag size (mm)	45	40	35	35
Undeformed length (cm)	15	14	13	13
Elongation ratio (%)	15	21	46	69
Max. bending angle (°)	45	55	57	70
Bending stiffness (N · m/°)[b]	0.260	0.190	0.145	0.085
Torsional stiffness (N · m/°)[b]	3.17	1.96	1.09	0.63

[a] The wall thickness of the internal honeycomb structure.
[b] Stiffness measured with all airbags pressurized at 1.5 bar.

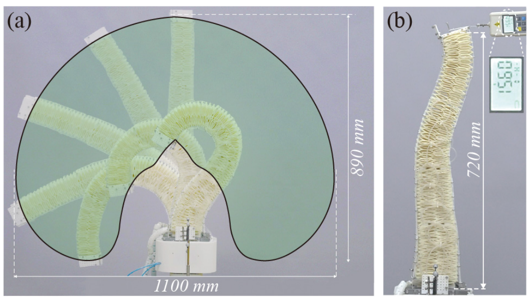

Fig. 3. Workspace and force output of the soft arm. (a) Reachable workspace envelope of the end-effector, spanning approximately 1100 mm laterally and 890 mm longitudinally under maximum bending and extension. (b) Measured force output in the vertical configuration, reaching 15.6 N and a corresponding bending moment exceeding 11 N·m.

torsional stiffness is 7–12 times the bending stiffness (Table I), letting the arm body itself serve as the torque-transmission path while remaining compliant in bending. The present prototype differs from the earlier arms in that its four-segment honeycomb frame is printed monolithically rather than fabricated segment-wise and mechanically joined; all mechanical properties reported in this paper were measured on this prototype.

Each segment contains four parallel airbag arrays: differential pressurization produces spatial bending and approximately uniform pressurization produces extension. The 16 arrays of the four segments are each regulated by a dedicated proportional valve. The frame is printed in flexible thermoplastic polyurethane (TPU), and the nylon-mesh-reinforced airbags operate up to 0.35 MPa. The arm measures 0.55 m undeformed and extends to approximately 0.76 m, with a proximal-to-distal compliance gradient (Table I); its workspace and force output are shown in Fig. 3.

Proximal rotation. Roll is driven by a vane-type pneumatic rotary actuator (PRA; Festo DRVS-32-270-P) providing a nominal torque of 7.5 N·m at 0.45 MPa over a 270° stroke (Fig. 2(d)); prior implementations of this architecture instead use motorized proximal rotation [12]–[14]. The PRA shares the arm's air supply, valve manifold and pneumatic control infrastructure; its direct-drive vane mechanism has no gear reduction and its compressible antagonistic chambers let the shaft yield under external torque, so the roll axis remains back-drivable, with its compliance set by the chamber bias pressure (Sec. IV-C).

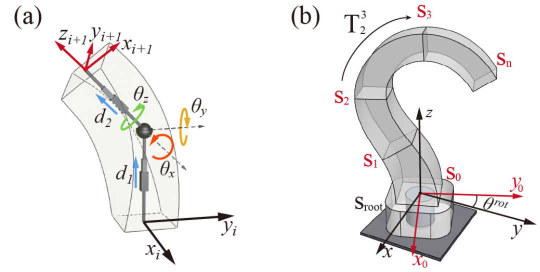

Fig. 4. Kinematic modeling of the arm. (a) Single-segment schematic showing bending (red and yellow), torsion (green), and extension (blue) deformation modes. (b) Kinematics of the multisegment soft arm and PRA, where S_{root} is the world frame and S_0 is the arm base frame after PRA rotation.

Because arm weight and payload generate substantial radial loads and bending moments at the base, a slewing bearing carries these loads while the PRA transmits primarily axial torque (Fig. 2(c)), protecting the cylinder shaft and seals and enabling smooth rotation under deflected configurations.

III. MODELING

We model the kinematics of the arm and base rotation with an explicit passive torsion coordinate per segment, then derive the task-space Jacobian and identify a sparse actuation Jacobian.

A. Forward Kinematics

*1) **Spherical Joint Model:*** Extending the universal-joint model in [16], we add a passive torsion coordinate θ_z^i and model each segment as a prismatic–spherical–prismatic chain (Fig. 4(a)). For $\boldsymbol{q}^i = [d_1^i, \theta_x^i, \theta_y^i, \theta_z^i, d_2^i]$, the segment pose is:

$$\boldsymbol{T}_{i-1}^i = \mathbf{T}_z(d_1^i)\mathbf{R}_y(\theta_y^i)\mathbf{R}_x(\theta_x^i)\mathbf{R}_z(\theta_z^i)\mathbf{T}_z(d_2^i), \tag{2}$$

where the translation operators $\mathbf{T}_z(d_1^i)$ and $\mathbf{T}_z(d_2^i)$ describe axial extension; the rotation operators $\mathbf{R}_x(\theta_x^i)$ and $\mathbf{R}_y(\theta_y^i)$ describe the bending configuration; and $\mathbf{R}_z(\theta_z^i)$ characterizes the passive torsional deformation θ_z^i.

*2) **Multisegment and System Model:*** For an n-segment arm, $\boldsymbol{q}^{arm} = [\boldsymbol{q}^1, \boldsymbol{q}^2, \ldots, \boldsymbol{q}^n] \in \mathbb{R}^{5n}$, and the end-effector pose relative to the arm base frame $\{S_0\}$ is:

$$\boldsymbol{T}^{arm} = \mathcal{K}_1(\boldsymbol{q}^{arm}) = \prod_{i=1}^{n} \boldsymbol{T}_{i-1}^i. \tag{3}$$

The base PRA adds $\boldsymbol{T}^{rot} = \mathbf{R}_z(\theta^{rot})$ (Fig. 4(b)). For $\boldsymbol{q} = [\theta^{rot}, \boldsymbol{q}^{arm}] \in \mathbb{R}^{5n+1}$, the world-frame end-effector pose is:

$$\boldsymbol{T} = \mathcal{K}_2(\boldsymbol{q}) = \boldsymbol{T}^{rot}\boldsymbol{T}^{arm}. \tag{4}$$

B. Task-Space Jacobian Derivation

Given the mapping $\boldsymbol{T} = \mathcal{K}(\boldsymbol{q})$, a change from $\boldsymbol{q}$ to $\boldsymbol{q}'$ results in a pose evolution from $\boldsymbol{T}$ to $\boldsymbol{T}'$. The relative transformation in the end-effector frame is:

$$\boldsymbol{T}_\Delta = \boldsymbol{T}^{-1}\boldsymbol{T}' = \begin{bmatrix} \boldsymbol{R}_{3\times3} & \boldsymbol{p}_{3\times1} \\ \mathbf{0}_{1\times3} & 1 \end{bmatrix}. \tag{5}$$

We define the decoupled local pose-error vector as:

$$\Delta\boldsymbol{x} = \left[\boldsymbol{p}^{\mathrm{T}}, \operatorname{Log}(\boldsymbol{R})^{\mathrm{T}}\right]^{\mathrm{T}} = [x, y, z, r_x, r_y, r_z]^{\mathrm{T}}, \tag{6}$$

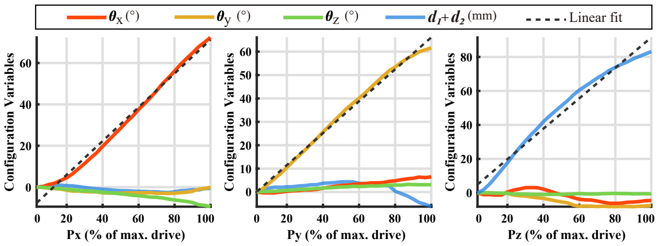

Fig. 5. Experimental identification of the actuation Jacobian for the distal segment. Independent equivalent actuation inputs are applied from the nominal vertical configuration over the calibrated 0–3 bar range (0%–100%): (a) bending under P_x, (b) bending under P_y, and (c) extension under P_z.

where $\mathrm{Log}(\boldsymbol{R}) \in \mathbb{R}^3$ is the axis–angle vector from the $SO(3)$ logarithm, equivalently computed by Rodrigues' formula [17].

The task Jacobian $\boldsymbol{J}_c \in \mathbb{R}^{6\times(5n+1)}$ in the end-effector frame is:

$$\boldsymbol{J}_c(\boldsymbol{q}) = \frac{\partial \Delta \boldsymbol{x}}{\partial \boldsymbol{q}} = \left[\, \nabla_{q_1}\Delta\boldsymbol{x}\,,\, \nabla_{q_2}\Delta\boldsymbol{x}\,,\,\cdots\,,\, \nabla_{q_{5n+1}}\Delta\boldsymbol{x} \,\right], \tag{7}$$

where each column $\nabla_{q_j}\Delta\boldsymbol{x} = [\frac{\partial x}{\partial q_j}, \frac{\partial y}{\partial q_j}, \frac{\partial z}{\partial q_j}, \frac{\partial r_x}{\partial q_j}, \frac{\partial r_y}{\partial q_j}, \frac{\partial r_z}{\partial q_j}]^{\mathrm{T}}$ represents the sensitivity of the 6D pose error to the j-th configuration variable, computed numerically column-by-column using finite differences.

C. Actuation-to-Configuration Mapping

For each segment i, the identified differential mapping uses equivalent bending and extension inputs $\boldsymbol{P}^i = [P_x^i, P_y^i, P_z^i]^{\mathrm{T}}$; their mapping from physical airbag pressures follows [3].

Under this definition, the dominant actuation–configuration relationships are $P_x^i \rightarrow \theta_x^i$, $P_y^i \rightarrow \theta_y^i$, and $P_z^i \rightarrow (d_1^i, d_2^i)$, while the torsion θ_z^i is passive and has no corresponding actuation input. Accordingly, the differential mapping is modeled by a sparse actuation Jacobian:

$$\Delta\mathbf{q}^i \approx \boldsymbol{J}_a^i \Delta\boldsymbol{P}^i, \qquad \boldsymbol{J}_a^i = \begin{bmatrix} 0 & 0 & \frac{\partial d_1^i}{\partial P_z^i} \\ \frac{\partial \theta_x^i}{\partial P_x^i} & 0 & 0 \\ 0 & \frac{\partial \theta_y^i}{\partial P_y^i} & 0 \\ 0 & 0 & 0 \\ 0 & 0 & \frac{\partial d_2^i}{\partial P_z^i} \end{bmatrix}. \tag{8}$$

The nonzero entries of $\boldsymbol{J}_a^i$ are the regression slopes in Fig. 5, obtained from independent inputs applied at the nominal vertical configuration over 0–3 bar; the same procedure is applied separately to each segment. The resulting fixed sparse matrix is used as an approximation under the calibrated quasi-static conditions and is not reidentified online.

IV. Control Strategy

Figure 6 shows the control framework. Global inverse kinematics (IK) computes goal configurations for the arm and the PRA, and PBKS turns them into synchronized references (Fig. 6(a)); the arm tracks its reference via state estimation and task-space feedback (Fig. 6(b)), and the PRA via angular PID control (Fig. 6(c)).

Algorithm 1 Progress-Based Kinematic Synchronization

Input: $\boldsymbol{q}_g^{arm}, \theta_g^{rot}, \boldsymbol{q}_n^{arm}, \theta_n^{rot}, \varepsilon_\phi, \varepsilon_\theta$
Parameter: $k_{\min} = 0.03$
Output: $\boldsymbol{q}_d^{arm}, \theta_d^{rot}$

1: **Azimuthal phase projection:**
$\phi_g^{arm} \leftarrow \Phi(\boldsymbol{q}_g^{arm}),\ \phi_n^{arm} \leftarrow \Phi(\boldsymbol{q}_n^{arm})$ ▷ (10)
2: **Progress coefficients:**
3: Define $\kappa(\delta, d; \varepsilon) \leftarrow \begin{cases} 1, & |d| < \varepsilon, \\ \mathrm{clip}\left(\frac{\delta}{d}, k_{\min}, 1\right), & \text{otherwise.} \end{cases}$
$k_i^{arm} \leftarrow \kappa(\phi_{n,i}^{arm} - \phi_{n,i-1}^{arm}, \phi_{g,i}^{arm} - \phi_{n,i-1}^{arm}; \varepsilon_\phi)$
$k_i^{rot} \leftarrow \kappa(\theta_{n,i}^{rot} - \theta_{n,i-1}^{rot}, \theta_{g,i}^{rot} - \theta_{n,i-1}^{rot}; \varepsilon_\theta)$
4: **Mutual guidance:**
$\theta_{d,i}^{rot} \leftarrow \theta_{d,i-1}^{rot} + k_i^{arm}(\theta_{g,i}^{rot} - \theta_{d,i-1}^{rot})$
$\phi_{d,i}^{arm} \leftarrow \phi_{d,i-1}^{arm} + k_i^{rot}(\phi_{g,i}^{arm} - \phi_{d,i-1}^{arm})$
5: **Arm target under phase constraint:**
$\boldsymbol{q}_{d,i}^{arm} = \arg\min_{\boldsymbol{q}} \ \|\boldsymbol{q} - \boldsymbol{q}_n^{arm}\|^2 \ \text{ s.t. } \ \Phi(\boldsymbol{q}) = \phi_{d,i}^{arm}$
6: **Return** $\boldsymbol{q}_{d,i}^{arm},\ \theta_{d,i}^{rot}$

A. Global IK and Synchronization

*1) **Global IK in the Actuated Subspace**:* Feedback-driven incremental control addresses soft-arm model error [3], [18], [19], but small PRA roll increments can remain below its stiction/deadband and produce stick–slip. We therefore compute a look-ahead global IK, reinitialized at each control update from $\boldsymbol{q}_n = [\theta_n^{rot}, \boldsymbol{q}_n^{arm}]$, where θ_n^{rot} is measured and $\boldsymbol{q}_n^{arm}$ is reconstructed in Sec. IV-B.1.

The relative transformation $\boldsymbol{T}_n^{-1}\boldsymbol{T}_g$ is mapped by (5)–(6) to the IK residual $\boldsymbol{\xi} \in \mathbb{R}^6$. Because $\{\theta_z^i\}$ are unactuated, global IK uses

$$\widetilde{\boldsymbol{J}}_c = \boldsymbol{J}_c\,\mathrm{diag}(\boldsymbol{d}), \qquad d_j = \begin{cases} 0, & j \in \{\,5k\,\}_{k=1}^{n}, \\ 1, & \text{otherwise.} \end{cases} \tag{9}$$

This projection zeros out the torsion columns and is used only in global IK; state estimation and local arm control retain them. Starting from $\boldsymbol{q}_n$, we apply the small-step update $\Delta\boldsymbol{q} = \alpha\widetilde{\boldsymbol{J}}_c^{\dagger}\boldsymbol{\xi}$, with $\alpha \ll 1$, and set $\boldsymbol{q} \leftarrow \boldsymbol{q} + \Delta\boldsymbol{q}$ until the residual threshold is met, yielding $\boldsymbol{q}_g = [\theta_g^{rot}, \boldsymbol{q}_g^{arm}]$.

*2) **Progress-Based Kinematic Synchronization (PBKS)**:* For arm-projection radius $\rho = \sqrt{(T_x^{arm})^2 + (T_y^{arm})^2}$, an uncompensated base rotation $\Delta\theta$ produces the lateral sweep $d_{\text{sweep}} = 2\rho\sin(|\Delta\theta|/2) \approx \rho|\Delta\theta|$ and velocity scale $v_{\text{sweep}} \approx \rho|\dot{\theta}^{rot}|$. The effect is therefore strongest at large radial offsets, motivating synchronous arm–PRA motion. We define the arm phase as

$$\phi^{arm} = \Phi(\boldsymbol{q}^{arm}) = \mathrm{atan2}(T_x^{arm},\ T_y^{arm}), \tag{10}$$

where T_x^{arm}, T_y^{arm} are expressed in $\{S_0\}$, so ϕ^{arm} is measured from $+y$ toward $+x$. The principal-valued atan2 has a branch cut at local $-y$; the reported tasks remain on one branch, and the current implementation does not unwrap crossings. Algorithm 1 advances each subsystem reference by the other's measured progress.

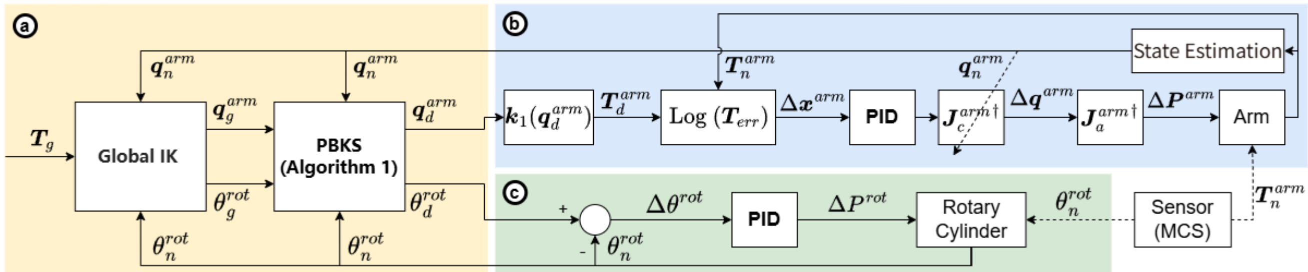

Fig. 6. Control framework. (a) Global IK and PBKS generate subsystem references. (b) Task-space control of the soft arm. (c) Angular control of the PRA.

In $\kappa()$, the positive lower bound starts mutual guidance from rest, while the upper bound prevents reverse or beyond-goal reference updates. The constrained arg-min seeks the configuration closest to the current estimate $\boldsymbol{q}_n^{arm}$ among those satisfying the target phase, minimizing arm motion. In real time, we do not solve it to optimality; instead, we apply small-step Jacobian-pseudoinverse updates from $\boldsymbol{q}_n^{arm}$ and return the first iterate reaching or crossing the target phase. Thus, the minimum-deviation solution is not guaranteed.

B. Soft Arm Task-Space Control

*1) **Soft-Arm State Estimation**:* State estimation reconstructs all arm coordinates $\boldsymbol{q}_n^{arm}$, including each passive $\theta_{z,n}^i$, from measured $\boldsymbol{T}_n^{arm}$ by reusing the small-step pseudoinverse iteration in Sec. IV-A. Starting from the nominal vertical $\boldsymbol{q}_0^{arm}$, it reduces the residual in (6) to the estimation threshold using the full torsion-aware $\boldsymbol{J}_c^{arm}$. The estimated θ_z^i values are latent model coordinates inferred from end-pose consistency, not segment-level sensor measurements or direct measurements of material twist; the PRA is excluded because θ_n^{rot} is measured independently.

*2) **Task-Space Feedback Control**:* To avoid configuration-space model error, $\boldsymbol{q}_d^{arm}$ is converted by forward kinematics to $\boldsymbol{T}_d^{arm}$ and the arm regulates the full 6D task-space error (Fig. 6(b)). Retaining the latent θ_z^i columns in the local pseudoinverse lets roll residuals be allocated away from large bending changes.

The soft arm is regulated using the 6D task-space error $\boldsymbol{e}_k = \Delta\boldsymbol{x}^{arm}$, constructed from the relative transformation $(\boldsymbol{T}_n^{arm})^{-1}\boldsymbol{T}_d^{arm} \in SE(3)$ according to the decoupled definition in Eq. (6).

$$\Delta\boldsymbol{q}^{arm} = (\boldsymbol{J}_c^{arm})^{\dagger}\left[K_p\Delta\boldsymbol{e}_k + K_i\boldsymbol{e}_k + K_d\delta^2\boldsymbol{e}_k\right], \quad (11)$$

where $\Delta\boldsymbol{e}_k = \boldsymbol{e}_k - \boldsymbol{e}_{k-1}$ and $\delta^2\boldsymbol{e}_k = \boldsymbol{e}_k - 2\boldsymbol{e}_{k-1} + \boldsymbol{e}_{k-2}$; $\boldsymbol{J}_c^{arm}$ denotes the arm-only task Jacobian, evaluated at the current configuration estimate $\boldsymbol{q}_n^{arm}$.

The corresponding pressure increment is obtained via the actuation Jacobian:

$$\Delta\boldsymbol{P}^{arm} = (\boldsymbol{J}_a^{arm})^{\dagger}\,\Delta\boldsymbol{q}^{arm}, \quad (12)$$

where $\boldsymbol{J}_a^{arm} = \boldsymbol{J}_a^1 \oplus \boldsymbol{J}_a^2 \cdots \oplus \boldsymbol{J}_a^n$. Its zero torsion rows prevent torsion components in $\Delta\boldsymbol{q}^{arm}$ from generating pressure commands, leaving roll regulation to the PRA.

C. Pneumatic Rotary Actuator (PRA) Angular Control

The PRA regulates the end-effector roll assigned by the global coordination loop. As shown in Fig. 6(c), for the target angle θ_d^{rot}, the angular error is defined as $e_k^{rot} = \Delta\theta^{rot} = \theta_d^{rot} - \theta_n^{rot}$. An incremental PID controller is used to compute the differential pressure increment:

$$\Delta P^{rot} = K_p^{rot}\,\Delta e_k^{rot} + K_i^{rot}\,e_k^{rot} + K_d^{rot}\,\delta^2 e_k^{rot}. \quad (13)$$

The two chamber pressures of the PRA are initialized with the same bias pressure p_b, which sets the average operating pressure and can be adjusted to tune the compliance of the PRA (lower p_b corresponds to a more compliant response). To implement antagonistic actuation while preserving this average pressure, the pressure increment is symmetrically allocated to the two chambers:

$$\begin{bmatrix} p_{r,k} \\ p_{l,k} \end{bmatrix} = \begin{bmatrix} p_{r,k-1} \\ p_{l,k-1} \end{bmatrix} + \frac{1}{2}\begin{bmatrix} 1 \\ -1 \end{bmatrix}\Delta P^{rot}, \quad (14)$$

where $p_{r,k}$ and $p_{l,k}$ denote the right and left chamber pressures (Fig. 2(d)) at time step k.

V. Experiments and Results

This section evaluates the proposed framework through three groups of experiments: workspace-wide 6-DoF pose regulation, independent roll (with the remaining five DoFs regulated) together with blocked-output roll torque, and three proof-of-concept roll-critical tasks.

Common experimental setup: All experiments used an OptiTrack Prime 13 motion-capture system (MCS) operating at 60 Hz to measure the end-effector pose and derive the PRA angle from rigid-body orientation; the controller was updated at 10 Hz. The measured static positional noise was approximately 0.2 mm. On a computer equipped with an AMD Ryzen 7 8845HS processor, all algorithmic calculations in one control cycle, including global IK, PBKS phase projection, and local control, averaged approximately 0.04 s, excluding sensor and actuator communication, below the 0.1 s control period.

A. Workspace-Wide 6-DoF Pose Regulation

The 30 target poses in Fig. 7(a) were randomly sampled from a hand-guided end-effector trajectory within the reachable workspace. Each target was approached from the common initial pose $[x, y, z, r_x, r_y, r_z] = [0, 450, 300, -90, 0, 0]$, where position and orientation are expressed in millimeters and degrees, respectively. A 30 s regulation interval was used

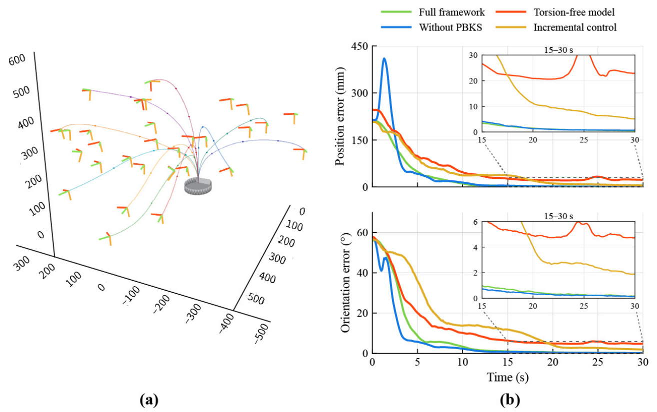

Fig. 7. Workspace-wide 6-DoF pose regulation over 30 target poses. (a) Schematic visualization of representative target poses and approximate arm configurations in the workspace. (b) Position and orientation errors averaged across the 30 targets for four control methods.

TABLE II

6-DoF POSE-REGULATION PERFORMANCE ACROSS 30 WORKSPACE TARGETS.

Control method	Metric	Over-shoot	Steady-state error	Threshold time (s) 50mm/10°	Threshold time (s) 5mm/2°	Failure rate
Full framework	Pos. (mm) Ori. (°)	8.06 0.39	0.59 ± 0.52 0.22 ± 0.29	5.0	12.0	0/30
w/o PBKS	Pos. (mm) Ori. (°)	211.51 7.71	0.71 ± 0.36 0.19 ± 0.13	3.7	12.3	0/30
Torsion-free model	Pos. (mm) Ori. (°)	44.08 6.50	24.55 ± 35.62 4.99 ± 8.27	10.2	> 30	16/30
Incremental control	Pos. (mm) Ori. (°)	20.27 8.66	6.15 ± 5.26 2.22 ± 2.16	16.7	> 30	13/30

for each target, followed by a 20 s return to the initial pose. The same target set was evaluated using the full framework, the framework with PBKS disabled, the framework with the torsion-free kinematic model, and incremental control. Incremental control uses the torsion-aware model and direct feedback-driven incremental updates without global IK or PBKS, while the PRA remains regulated by its independent angular PID loop. All four methods used the same PID gains, bias pressures, pressure limits, and 10 Hz update rate.

Table II reports the across-target mean overshoot, steady-state error, two joint threshold times, and high-accuracy failure rate. For each trial, i.e., one method on one target, overshoot was computed as $\max_t e(t) - e(0)$ and clipped at zero. Steady-state error was averaged over the final 5 s, after which the mean ± sample standard deviation was calculated across targets. The joint threshold time $T_{a\text{mm}/b^\circ}$ is the first time at which both across-target mean error curves enter and remain below a mm and $b°$, respectively. We report $T_{50\text{mm}/10^\circ}$ for coarse convergence and $T_{5\text{mm}/2^\circ}$ for fine-accuracy convergence. A trial was counted as a high-accuracy failure if, at $t = 30$ s, it did not simultaneously satisfy $e_p \leq 5$ mm and $e_R \leq 2°$; the failure rate is reported as $N_{\text{fail}}/30$.

Disabling PBKS increased the across-target mean position overshoot from 8.06 mm to 211.51 mm and the orientation overshoot from 0.39° to 7.71°, while the full and no-PBKS variants retained comparable steady-state errors. The full framework satisfied $e_p \leq 2$ mm and $e_R \leq 1°$ at $t = 30$ s for all 30 targets. Under the high-accuracy failure criterion, the torsion-free model and incremental control failed on 16/30 and 13/30 targets, respectively. These results support PBKS primarily as a transient-response mechanism and the torsion-aware global allocation as important for final accuracy over the tested workspace.

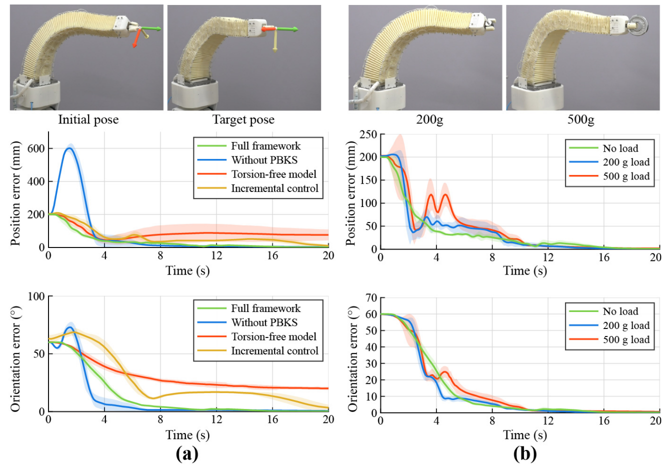

Fig. 8. Repeated 6-DoF pose regulation at a representative target.The initial and target poses differ by 200 mm in position and 60° in roll. (a) Mean position and orientation errors of the four control methods over 10 trials each; the photographs show the initial and target poses. (b) Mean errors of the full framework with no added payload and with 200 g and 500 g end-effector payloads over 10 trials per condition; the photographs show the arm at the target pose carrying each payload. Shaded bands indicate +1 standard deviation across trials.

Repeated comparison at a representative target: Across-target averaging can obscure controller differences and trial-to-trial variation at an individual command. We therefore repeated a representative target for 10 trials per method (Fig. 8(a)). Without PBKS, the mean position error first grows from the initial 200 mm to approximately 600 mm within 2 s instead of decreasing, an overshoot exceeding 400 mm; the full framework keeps the overshoot below 1 mm, and both reach comparable final accuracy. The wide position-error standard-deviation band of the torsion-free model indicates substantial trial-to-trial variation under the same command. Incremental control is more consistent than the torsion-free model but converges more slowly than the full framework.

To examine load sensitivity at the same representative target, we additionally evaluated the full framework with no added payload and with 200 g and 500 g end-effector payloads (Fig. 8(b)). At $t = 20$ s, the mean position errors were 1.03, 0.84, and 1.84 mm, respectively; all three remained below 2 mm under the tested conditions.

B. Independent Roll under Five-DoF Constraints

*1) **Independent-Roll Trajectory Tracking**:* This experiment isolates the roll capability enabled by proximal roll generation and transmission through the arm body. The end

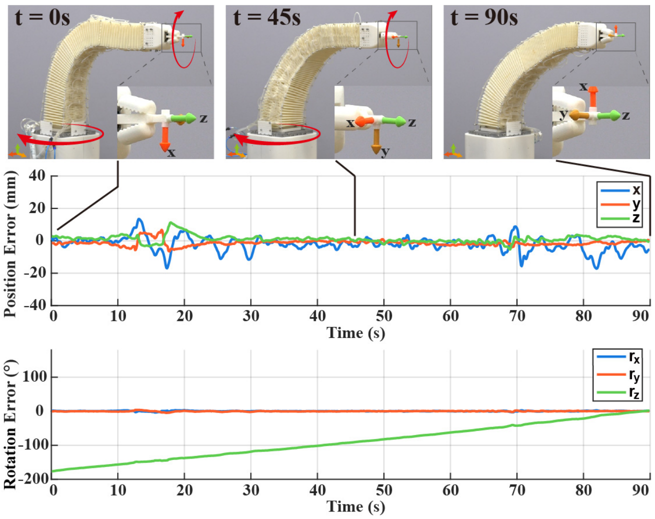

Fig. 9. Independent-roll trajectory tracking. The end-effector executes a 180° rotation about its roll axis while the other five DoFs are regulated at their initial values.

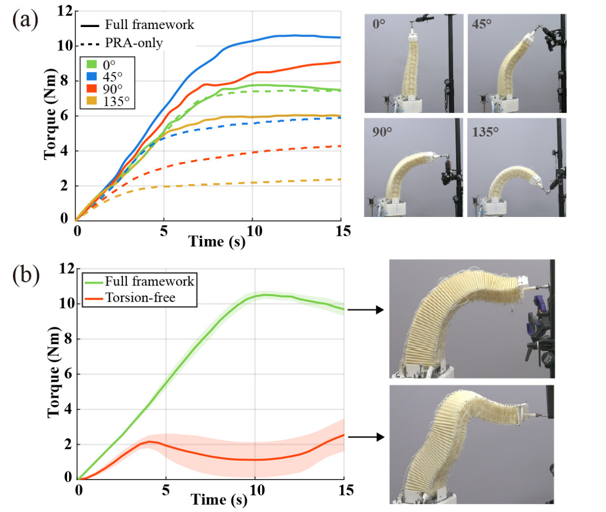

Fig. 10. Blocked-output roll-torque characterization. (a) Torque at four deflection angles for the full framework (solid) and PRA-only actuation with zero arm pressure (dotted); the photographs show the arm postures at $t = 15$ s. (b) Mean torque over five trials for the full framework and torsion-free model at $\beta = 90°$; shaded bands indicate the standard deviation, and the photographs show the corresponding postures at $t = 15$ s.

effector was commanded to execute a time-indexed 180° roll while its position and the other two orientation components were regulated at their initial values.

Throughout the motion, the average position and non-roll orientation errors were 4.8 mm and 1.0°, respectively, with transient position deviations visible in Fig. 9. The measured trajectory shows that independent roll was executed while the remaining five DoFs were regulated over the tested motion.

*2) **Blocked-Output Roll Torque Characterization**:* In both blocked-output tests, the end effector was rigidly connected to a torque sensor, which constrained rotation about the tool axis and measured the reaction torque about that axis. After the target bending posture was established, the controller followed discretized references for a commanded 60° roll at 6°/s. The deflection angle β is the angle between the end-effector pointing axis and the world-frame z-axis. The target in Fig. 10(a) was closer to the arm base so that the locked end constraint could maintain the bent posture for the PRA-only baseline with zero arm pressure; the target in Fig. 10(b) was slightly more distal to maintain stable control with the torsion-free model. This target difference accounts for the small difference between the full-framework values at $\beta = 90°$.

The posture sweep covers $\beta \in \{0°, 45°, 90°, 135°\}$ (Fig. 10(a)). For the PRA-only baseline, the arm chambers remained at zero pressure and the PRA was driven to its nominal saturation torque of 7.5 N·m. At $t = 15$ s, the measured end-effector torque was 7.5 N·m at $\beta = 0°$ and decreased as β increased.

With the full framework, the measured blocked-output roll torque at $t = 15$ s exceeded 6 N·m in all four postures and reached 10.5 N·m at $\beta = 45°$. Relative to the PRA-only baseline with zero arm pressure at the corresponding postures, the measured blocked-output roll torques were higher by factors of 1.01, 1.78, 2.13, and 2.53, respectively. Under the locked-end constraint, the measured axial reaction torque at the end effector includes contributions from the PRA

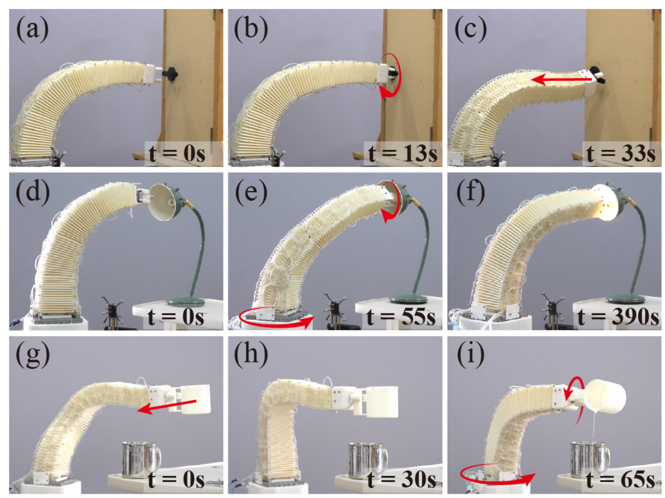

Fig. 11. Proof-of-concept roll-critical tasks. (a–c) Door unlocking, (d–f) lightbulb installation, and (g–i) water pouring.

and the actively pressurized bending segments. It therefore characterizes coordinated whole-body roll-torque generation, rather than unchanged transmission or amplification of the PRA's nominal torque.

In Fig. 10(b), the absence of passive torsion coordinates causes the torsion-free controller to allocate the roll residual to combined segment bending. The resulting posture distortion accompanies a fluctuating reaction torque below approximately 3 N·m, whereas the full framework maintains a more consistent posture and reaches approximately 10 N·m at the tested constrained posture.

C. Proof-of-Concept Roll-Critical Tasks

Fig. 11 qualitatively demonstrates the three roll-critical tasks motivated in Sec. I (see also the accompanying video). MCS markers on each object define an object frame, and a pre-calibrated transform maps the measured object pose to the key poses of the task, such as the grasp pose on the door handle. The controller then regulates the end effector through a predefined sequence of target poses expressed relative to the object.

Door unlocking: The handle must be turned while the grasp on it is maintained, which requires rolling the end effector in place. The arm approached and grasped the handle (Fig. 11(a)), turned it (Fig. 11(b)), and pulled it backward (Fig. 11(c)).

Lightbulb installation: Screwing in the bulb requires rolling it while keeping it coaxial with the socket. After the bulb was aligned with and inserted into the socket (Fig. 11(d)), the controller applied three preset 200° roll strokes (Fig. 11(e)). Between strokes, the bulb was released, the PRA was reset, and the bulb was regrasped; this release-and-reset sequence extended the total roll to 600°, beyond the 270° PRA stroke, after which the bulb lit (Fig. 11(f)).

Water pouring: Pouring requires tilting the container by rolling the end effector while its position is held above a target cup. The arm translated a container holding 500 mL of water by 30 cm to a position above the cup (Fig. 11(g)–(h)), and the end effector then rolled to pour the water (Fig. 11(i)).

VI. Discussion and Conclusion

A. Discussion

The framework was evaluated only under quasi-static operation; higher-speed manipulation would require a dynamics-aware model incorporating arm inertia, structural damping, and pneumatic flow. The reported slow trajectories therefore do not establish control bandwidth or dynamic stability. The spherical-joint approximation exhibits Cardan-like velocity non-uniformity, for which a constant-velocity formulation could reduce the transient position deviations observed during independent roll. The PRA provides 270° per stroke and supports larger finite rotations through release-and-reset sequences, whereas continuous rotation requires alternative actuation. PBKS uses the principal atan2 value within a single phase branch; a trajectory crossing the arm-base negative y-axis would require phase unwrapping, which is not included in the current implementation. Lightbulb thread engagement relies on position control alone; force or tactile feedback could make alignment more robust in precision assembly. More broadly, workspace-boundary and overload behavior remain to be systematically characterized.

B. Conclusion

We presented closed-loop regulation of all six end-effector pose coordinates on a fully pneumatic soft manipulator whose roll is generated at the arm base and transmitted through the arm body, extending this architecture from surgical-scale, mN·m systems to manipulation scale. Explicit passive torsion coordinates keep arm-side roll residuals from being misallocated to active bending, and progress-based synchronization suppresses the transient sweep left by base–arm progress mismatch. Across 30 workspace targets under four control configurations, the full framework satisfied 2 mm / 1° at t = 30 s at every target, against 16 failures for a torsion-free model, and blocked-output tests measured 6 –10.5 N·m of end-effector roll torque. Door unlocking, lightbulb installation and water pouring demonstrate the resulting task repertoire.

References

[1] D. Rus and M. T. Tolley, "Design, fabrication and control of soft robots," *Nature*, vol. 521, no. 7553, pp. 467–475, 2015.

[2] C. Laschi, B. Mazzolai, and M. Cianchetti, "Soft robotics: Technologies and systems pushing the boundaries of robot abilities," *Science Robotics*, vol. 1, no. 1, p. eaah3690, 2016.

[3] H. Jiang, Z. Wang, Y. Jin, X. Chen, P. Li, Y. Gan, S. Lin, and X. Chen, "Hierarchical control of soft manipulators towards unstructured interactions," *The International Journal of Robotics Research*, vol. 40, no. 1, pp. 411–434, 2021.

[4] X. Huang, J. Zou, and G. Gu, "Kinematic modeling and control of variable curvature soft continuum robots," *IEEE/ASME Transactions on Mechatronics*, vol. 26, no. 6, pp. 3175–3185, 2021.

[5] J. Liu, Z. Song, Y. Lu, H. Yang, X. Chen, *et al.*, "An underwater robotic system with a soft continuum manipulator for autonomous aquatic grasping," *IEEE/ASME Transactions on Mechatronics*, vol. 29, no. 2, pp. 1007–1018, 2024.

[6] S. Behl, C. Escande, P. M. Pathak, R. Merzouki, and B. K. Mishra, "Dynamic modelling of multi section bionic manipulator: Application to Robotino-XT," in *Proceedings of the 6th International Conference on Integrated Modeling and Analysis in Applied Control and Automation*, 2012, pp. 247–252.

[7] S. Frieler, J.-P. P. M. de Vries, S. Misra, and V. K. Venkiteswaran, "MAGTWIST: A magnetically-driven rotary actuator using a traveling-wave with integrated stiffness tunability," *Advanced Functional Materials*, vol. 36, no. 31, p. e27009, 2026.

[8] P. Yuan, C. Sun, X. Chang, X. Dong, Z. Song, T. Sun, J. S. Dai, and R. Kang, "Design of a deployable continuum robot (DCR) with coiling mechanism," *IEEE/ASME Transactions on Mechatronics*, vol. 30, no. 6, pp. 4886–4898, 2025.

[9] P. Yuan, C. Sun, X. Chang, X. Zhang, and R. Kang, "Enhancing continuum robot mobility: Design and control with integrated dual rotational DoFs," in *2025 IEEE/RSJ International Conference on Intelligent Robots and Systems (IROS)*. IEEE, 2025, pp. 3287–3292.

[10] M. Carton, J. F. Kowalewski, J. Guo, J. F. Alpert, A. Garg, D. Revier, and J. I. Lipton, "Bridging hard and soft: Mechanical metamaterials enable rigid torque transmission in soft robots," *Science Robotics*, vol. 10, no. 100, p. eads0548, 2025.

[11] Y. Kong, S. Song, N. Zhang, J. Wang, and B. Li, "Design and kinematic modeling of in-situ torsionally-steerable flexible surgical robots," *IEEE Robotics and Automation Letters*, vol. 7, no. 2, pp. 1864–1871, 2022.

[12] Q. Zhao, J. Lai, X. Hu, and H. K. Chu, "Dual-segment continuum robot with continuous rotational motion along the deformable backbone," *IEEE/ASME Transactions on Mechatronics*, vol. 27, no. 6, pp. 4994–5004, 2022.

[13] Q. Zhao, S. Wang, J. Hu, H. Liu, and H. K. Chu, "Controller design for a soft continuum robot with concurrent continuous rotation," *IEEE/ASME Transactions on Mechatronics*, vol. 29, no. 6, pp. 4504–4513, 2024.

[14] Y. Gao, D. Cheng, H. Dong, Z. Du, W. Wang, Y. Su, and W. Dong, "Design and control of continuum manipulators with pose reconstruction based on feedforward compensation," *IEEE Transactions on Medical Robotics and Bionics*, vol. 8, no. 1, pp. 264–276, 2026.

[15] H. Jiang, X. Liu, X. Chen, Z. Wang, Y. Jin, and X. Chen, "Design and simulation analysis of a soft manipulator based on honeycomb pneumatic networks," in *2016 IEEE International Conference on Robotics and Biomimetics (ROBIO)*. IEEE, 2016, pp. 350–356.

[16] Z. Wang, G. Wang, X. Chen, and N. M. Freris, "Kinematic modeling and control of a soft robotic arm with non-constant curvature deformation," in *2024 IEEE International Conference on Robotics and Automation (ICRA)*. IEEE, 2024, pp. 12 749–12 755.

[17] K. M. Lynch and F. C. Park, *Modern Robotics: Mechanics, Planning and Control*. Cambridge University Press, 2017.

[18] M. C. Yip and D. B. Camarillo, "Model-less feedback control of continuum manipulators in constrained environments," *IEEE Transactions on Robotics*, vol. 30, no. 4, pp. 880–889, 2014.

[19] Y. Jin, Y. Wang, X. Chen, Z. Wang, X. Liu, H. Jiang, and X. Chen, "Model-less feedback control for soft manipulators," in *2017 IEEE/RSJ International Conference on Intelligent Robots and Systems (IROS)*. IEEE, 2017, pp. 2916–2922.